Title

Multimodal Nonlinear Hyperspectral Chemical Imaging Using Line-Scanning Vibrational Sum-Frequency Generation Microscopy.

Authors

Wagner, Jackson

Yang, Bin

Wu, Zishan

et al.

Publication Date

2023-12-01

DOI

10.3791/65388

Peer reviewed

HHS Public Access

Author manuscript

J Vis Exp. Author manuscript; available in PMC 2024 March 01.

Multimodal Nonlinear Hyperspectral Chemical Imaging Using Line-scanning Vibrational Sum-frequency Generation Microscopy

Jackson C. Wagner[1], **Bin Yang**[1,2], **Zishan Wu**[1], **Wei Xiong**[1,3,4,*]

[1]Department of Chemistry and Biochemistry, UC San Diego, La Jolla, CA, United States

[2]State Key Laboratory of Molecular Reaction Dynamics, Dalian Institute of Chemical Physics, Chinese Academy of Sciences, Dalian, P. R. China

[3]Materials Science and Engineering Program, UC San Diego, La Jolla, CA, United States

[4]Department of Electrical and Computer Engineering, UC San Diego, La Jolla, CA, United States

Abstract

Vibrational sum-frequency generation (VSFG), a second-order nonlinear optical signal, has traditionally been used to study molecules at interfaces as a spectroscopy technique with a spatial resolution of ~100 μm. However, the spectroscopy is not sensitive to the heterogeneity of a sample. To study mesoscopically heterogeneous samples, we, along with others, pushed the resolution limit of VSFG spectroscopy down to ~1 μm level and constructed the VSFG microscope. This imaging technique not only can resolve sample morphologies through imaging, but also record a broadband VSFG spectrum at every pixel of the images. Being a second-order nonlinear optical technique, its selection rule enables the visualization of non-centrosymmetric or chiral self-assembled structures commonly found in biology, materials science, and bioengineering, among others. In this article, the audience will be guided through an inverted transmission design that allows for imaging unfixed samples. This work also showcases that VSFG microscopy can resolve chemical-specific geometric information of individual self-assembled sheets by combining it with a neural network function solver. Lastly, the images obtained under brightfield, SHG, and VSFG configurations of various samples briefly discuss the unique information revealed by VSFG imaging.

SUMMARY:

A multimodal, rapid hyperspectral imaging framework was developed to obtain broadband vibrational sum-frequency generation (VSFG) images, along with brightfield, second harmonic generation (SHG) imaging modalities. Due to the infrared frequency being resonant with molecular vibrations, microscopic structural and mesoscopic morphology knowledge is revealed of symmetry-allowed samples.

*corresponding author: Wei Xiong (w2xiong@ucsd.edu).

A complete version of this article that includes the video component is available at http://dx.doi.org/10.3791/65388.

DISCLOSURES:
The authors have nothing to disclose.

Keywords

infrared imaging; nonlinear optics; structure-property; self-assembly; vibrational sum-frequency generation; sum-frequency generation microscopy; hyperspectral imaging; material characterization; hierarchical organization

INTRODUCTION:

Vibrational sum-frequency generation (VSFG), a second-order nonlinear optical technique[1,2], has been used extensively as a spectroscopy tool to chemically profile symmetry-allowed samples[3–22]. Traditionally, VSFG has been applied to interfacial systems[8–11] (i.e., gas-liquid, liquid-liquid, gas-solid, solid-liquid), which lack inversion symmetry – a requirement for VSFG activity. This application of VSFG has provided a wealth of molecular details of buried interfaces[12,13], configurations of water molecules at interfaces[14–18], and chemical species at interfaces[19–22].

Although VSFG has been powerful in determining molecular species and configurations at interfaces, its potential in measuring molecular structures of materials lacking inversion centers has not been fulfilled. This is partly because the materials could be heterogeneous in their chemical environment, compositions, and geometric arrangement, and a traditional VSFG spectrometer has a large illumination area on the order of 100 μm^2. Thus, traditional VSFG spectroscopy reports on ensemble-averaged information of the sample over a typical 100 μm^2 illumination area. This ensemble averaging may lead to signal cancellations between well-ordered domains with opposite orientations and mischaracterization of local heterogeneities[15,20,23,24].

With advances in high numerical aperture (NA), reflective-based microscope objectives (Schwarzschild and Cassegrain geometries), which are nearly free of chromatic aberrations, the focus size of the two beams in VSFG experiments can be decreased from 100 μm^2 to 1–2 μm^2 and in some cases submicron[25]. Including this technological advancement, our group and others have developed VSFG into a microscopy platform[20,23,26–36]. Recently, we have implemented an inverted optical layout and broadband detection scheme[37], which enables a seamless collection of multimodal images (VSFG, second harmonic generation (SHG), and brightfield optical). The multimodality imaging allows quick inspection of samples using optical imaging, correlating various types of images together, and locating signal positions on the sample images. With the achromatic illumination optics and choice of pulsed laser illumination source, this optical platform allows for future seamless integration of additional techniques such as Fluorescence microscopy[38] and Raman microscopy, among others.

In this new arrangement, samples such as hierarchical organizations and a class of molecular self-assemblies (MSAs) have been studied. These materials include collagen and biomimetics, where both the chemical composition and geometric organization are important to the ultimate function of the material. Because VSFG is a second-order nonlinear optical signal, it is specifically sensitive to intermolecular arrangements[39,40], such as intermolecular distance or twisting angles, making it an ideal tool for revealing both chemical compositions and molecular arrangements. This work describes the VSFG,

SHG, and brightfield modalities of the core instrument consisting of a ytterbium-doped cavity solid-state laser that pumps an optical parametric amplifier (OPA), a home-built multimodal inverted microscope and monochromator frequency analyzer coupled to a two-dimensional charged coupled device (CCD) detector[27]. A step-by-step construction and alignment procedures, and a complete part list of the setup, are provided. An in-depth analysis of an MSA, whose fundamental molecular subunit is comprised of one molecule of sodium-dodecyl sulfate (SDS), a common surfactant, and two molecules of β-cyclodextrin (β-CD), known as SDS@2β-CD herein, are also provided as an example to show how VSFG can reveal molecule-specific geometric details of organized matter. It has also been demonstrated that chemical-specific geometric details of the MSA can be determined with a neural network function solver approach.

PROTOCOL:

1. Hyperspectral line-scanning VSFG microscope

1.1. Laser system

1.1.1. Use a pulsed laser system (see Table of Materials) centered at 1025 nm ± 5 nm. The laser is set at 40 W, 200 kHz (200 μJ/pulse) with a pulse width of ~290 fs.

NOTE: The exact repetition rate can vary, and a high repetition rate laser generally works better for this VSFG microscope.

1.1.2. Guide the output of the seed laser into a commercial optical parametric amplifier (OPA) to generate a mid-infrared (MIR) beam (see Table of Materials). Tune the MIR to the frequency of interests (Figure 1A).

NOTE: In the present study, the MIR is centered at 3450 nm ± 85 nm (~2900 ± 72 cm^{-1}) with a pulse duration of ~290 fs and pulse energy of ~6 μJ, which encompasses part of the $-CH_x$ functional group region.

1.2. Up-conversion beam

1.2.1. Pass the residual 1025 nm beam from OPA through a Fabry-Perot etalon (see Table of Materials) to produce a spectrally narrowed up-conversion beam with an FWHM of ~4.75 cm^{-1}.

1.2.2. Spatially filter the narrowed 1025 nm beam with an 8 μm sapphire pinhole.

NOTE: The 1025 nm beam can be visualized using a NIR card.

1.2.3. Control the polarization of the 1025 nm pulse with a λ/2 waveplate (see Table of Materials).

1.3. MIR beam

1.3.1. Guide the MIR beam through a delay stage for fine control of the temporal overlap.

1.3.2. Control the polarization of the MIR with a λ/2 waveplate.

1.4. VSFG microscope

1.4.1. Spatially overlap both up-conversion, and MIR beams at a customized dichroic mirror (DM, Figure 1B) that is transmissive to MIR and reflective to NIR (see Table of Materials). Use two irises to guide the alignment: one right after the DM, and one at the far end. Use a power meter after the iris to determine whether MIR is centered, and use a NIR card to locate NIR positions.

NOTE: After the overlap, the NIR beam can be used to guide both beams.

1.4.2. Direct the overlapped beams into an inverted microscope with an integrated 325 Hz single-axis resonant beam scanner (mounted to an integrated two-position scanner (I2PS), Figure 1B) (see Table of Materials).

NOTE: The resonant scanner projects a line of the two overlapped beams onto the back aperture of the condenser objective. It is mounted to a slider which enables the seamless reconfiguration between VSFG/SHG and brightfield modalities.

1.4.3. Focus the two spatially overlapped beams onto the sample with a purely reflective Schwarzschild objective (SO, Figure 1B,D) (see Table of Materials).

1.4.4. Collect the VSFG signal generated by the sample with an infinity-corrected refractive objective (RO, Figure 1B,D) (see Table of Materials).

1.4.5. Guide the collimated output VSFG signal through a linear polarizer and then through a telecentric tube lens system composed of two f = 60 mm focal lenses (TL1 and TL2, Figure 1B,C) (see Table of Materials).

NOTE: The magnified image from the tube lenses is formed at the entrance slit of the monochromator (MC, Figure 1B,C), and the spatially/frequency resolved data is detected on a two-dimensional CCD detector (CCD, Figure 1B).

1.5. SHG mode

1.5.1. To switch to SHG imaging, block the IR beam and rotate the grating of the spectrograph to 501.5 nm to image the SHG signal.

1.6. Brightfield mode

1.6.1. To switch to brightfield optical imaging, turn on the whitelight source (see Table of Materials). Move the integrated slider (I2PS, Figure 1B) to collect brightfield images in the counter-propagating direction, with the imaging objective (RO) acting as the condenser and the condenser objective (SO) acting as the imaging objective.

1.6.2. Form an image of the collimated output of the refractive objective at the sensor plane of an RGB brightfield camera using a commercially available tube-lens system (see Table of Materials).

2. Hyperspectral microscope alignment and vertical CCD axis spatial calibration

2.1. Roughly optimize the position of the sample plane (nano positioner z-axis) using a standard sample of ZnO (1 μm thick) pattern sputter coated 15 mm x 15 mm x 0.170 mm ± 0.005 mm coverslip and bringing it into brightfield focus using the brightfield imaging modality.

NOTE: The z-position of the RO as well as the alignment of the white light, may need to be adjusted as necessary. A representative image of the ZnO on the glass pattern used for alignment calibration is shown in Figure 2.

2.2. Move the I2PS back to the nonlinear illumination arm and optimize the sample height for the maximum nonresonant VSFG intensity generated by the ZnO regions observed on the CCD camera.

NOTE: The z-position of the RO must be adjusted for maximum intensity. One may have to iterate steps 2.1 and 2.2 a few times before the optimal height of the sample, and RO are reached.

2.3. Turn the resonant beam scanner on and collect a line of the images.

2.4. Collect nonresonant intensity images by scanning the sample perpendicularly to the beam scanner direction. Take vertical slices of the image data and establish the pixel:micron ratio. (refer to Figure 3 and its legend).

NOTE: The derivative of these line sections is analyzed to produce the vertical CCD axis pixel:micron ratio that will be used for future images.

3. Hyperspectral data collection

3.1. Collect the spectra of a vertical line of the VSFG signals on the CCD, whose spectra are dispersed along the horizontal axis and spatial positions are recorded on the vertical axis of the CCD.

NOTE: This results in a two-dimensional data set for a single-line section.

3.2. After the line section of the sample is hyperspectrally imaged, scan the sample in the axis perpendicular to the line scanning axis using the three-dimensional nano-positioner (NP, Figure 1).

NOTE: The 3D nano positioner is important for high precision and reproducibility in locating sample regions (x-y plane) as well as bringing the sample into focus (z-axis).

3.3. Iterate between step 3.1 and step 3.2 to collect a VSFG hyperspectral image.

4. Hyperspectral data analysis

4.1. Spectrally unmix the data using the MatLab imaging toolbox hyperspectral imaging library workflow[41].

NOTE: Spectral unmixing correlates spatial locations to unique spectra. Matlab code for hyperspectral data analysis is provided in Supplementary File 1.

4.1.1. Create a 4-dimensional hypercube (x = spatial, y = spatial, z = frequency-dependent intensity, ω = frequency) using the **hypercube** function in the Matlab image processing toolbox hyperspectral imaging library[41].

4.1.2. Identify the number of unique spectra with the **countEndmembersHFC** function with a probability of false alarm (PFA) value of 10^{-7}.

4.1.3. Identify unique spectra using the **nfindr** spectral unmixing function.

4.1.4. Finally, using the **sid** function, associate each pixel with one of the unique spectra identified in the previous step.

NOTE: Additional spectral unmixing and matching methods can be done with alternative functions/algorithms offered in the MatLab Hyperspectral Imaging Library[41].

4.2 **Fit** the sum data for each isolated sheet to the Voigt function[42] (Supplementary File 1).

NOTE: Lorentzian function represents the pure homogeneous lineshape limit, whereas the Gaussian function originates from inhomogeneous limits. In reality, the systems could be in a combination of homogeneous and inhomogeneous limits, which requires a Voigt function – a common practice for condensed phase spectroscopy, including VSFG.

5. Geometric analysis of the sample

5.1. Determine the geometry of the samples following the procedure mentioned in step 5.2-5.3. In this study, SDS@2β-CD is used as an example. Derive the symmetry-allowed tensor elements of $\chi^{(2)}$ based on the C_7 symmetry of the molecular subunit of the SDS@2β-CD meso-sheets sample.

NOTE: The symmetry allowed $\chi^{(2)}$ depends on symmetry. To calculate the allowed nonlinear susceptibility of any symmetry, refer to reference[43].

5.2. Apply the Euler rotation[27] to relate the lab frame measurements to the molecular frame.

NOTE: In the case of SDS@2β-CD, its C_7 symmetry leads to eight independent equations relating 8 output (lab frame $\chi^{(2)}$) to 8 input (6 independent hyperpolarizability $\beta^{(2)}$ and two angles: Θ, the tilt angle relative to the sample plane of all sheets, and ϕ, the in-plane rotation of the sheet (Figure 4)). Two sheets are used to extract the common molecular alignments of the two sheets. The relationships between ϕ_1 and ϕ_2 (in-plane rotation angle of the two sheets) can be extracted from the brightfield images. In the current example, $\phi_2 = \phi_1 + 60°$. It is assumed that all molecular unit tile at the same angle, so $\Theta_1 = \Theta_2$. This results in 11 unknowns (9 independent ones, including 6 independent hyperpolarizability $\beta^{(2)}$, Θ_1 and ϕ_1, and the relative coverage ratio between sheets N, and the two dependent angles, that are ϕ_2, and Θ_2) for 16 knowns (8 lab frame polarizations per sheet, and two sheets).

5.3. Relate the polarization-resolved lab frame $\chi^{(2)}$ and molecular frame hyperpolarizability $\beta^{(2)}$ with a neural network function solver.

NOTE: A detailed summary of this approach can be found in reference[27].

5.3.1. Create a layered neural network model in Python[44] using Keras comprised of 200-100-50 node structure and a hyperbolic tangent activation function.

5.3.2. Create a randomly generated 100000 x 11 matrix of values of $\beta^{(2)}$ Θ_1, Θ_2, ϕ_1, ϕ_2 and N. Calculate the corresponding lab frame 16 $\chi^{(2)}$, using the equation determined in 5.2 by Euler rotations.

5.3.3. Use the calculated $\chi^{(2)}$ values (a total of 100,000 by 16 values) as the input, and learn to predict 11 values ($\beta^{(2)}$, Θ_1, Θ_2, ϕ_1, ϕ_2 and N) when supplied 16 $\chi^{(2)}$ values.

5.3.4. Once trained, use another set of 1000 entries with both the inputs and outputs to test the trained model. The predicted output and the true output should show a linear relationship with a slope of 1.

5.3.5. Lastly, supply the experimentally measured $\chi^{(2)}$ from two sheets (each sheet have 8 $\chi^{(2)}$ measured), and use the trained model to predict the tilt angle Θ, along with other properties.

REPRESENTATIVE RESULTS:

The ability of the microscope to discriminate between uniquely organized molecular structures and isotropic bulk is demonstrated with the SDS@2β-CD sample[23,34] (Figure 5). In this study, the sample was prepared by adding β-CD and SDS to deionized water (DI) water at 2:1 ratio until the two solutes reached a 10% m/m concentration. The suspension was then heated to clarity and cool to room temperature overnight. $CuCl_2$ was added at a concentration of 1:10 $CuCl_2$:SDS to tune the electrostatic interactions and the mixture was allowed to sit for 3–5 days for SDS@2β-CD meso-sheets to form fully. Lastly, isolated meso-sheets were produced by drop casting 5 μL of the sheet suspension onto a 15 mm x 15 mm x 0.170 mm ± 0.005 mm coverslip affixed to a spin coater operating at 10,000 rpm.

The mesoscale sheets formed from their self-assembly with a specific C_7 symmetry. Yet, it is unclear about the molecular orientation of the single molecular unit in this self-assembly, a fundamental knowledge that can influence the material functions. (Figure 5C). VSFG images of the self-assembled sheets dispersed on a coverslip were captured (Figure 6A). Through spectral identification (step 4 Hyperspectral data analysis) using the Matlab hyperspectral imaging function, it was found that all sheets can be categorized into two types, one with higher VSFG intensity (blue spectra in Figure 6B, and sheets labeled in blue in Figure 6A), and the other one with lower intensity. By inspecting and comparing with the optical image (Figure 6C,D), the large sheet at the center of the images appeared to have stacked double sheets, thereby attributing the smaller VSFG intensity due to destructive interference between the two different orientation sheets. The single sheet was focused to extract the single molecular unit orientation (blue ones in Figure 6A). Two of

the sheets (highlighted in red and blue squares in Figure 6A) were measured by various VSFG polarizations, and the spectra were fitted using the Voigt functions. Note the VSFG polarization is described in the order signal, up-conversion and MIR. For example, SSP means P polarization of IR, S polarization of up-conversion and S polarization of signals.

Then, to extract the molecular orientations, the symmetry-allowed hyperpolarizability, $\beta_{ijk}^{(2)}$ was first determined, allowed by the symmetry selection rule, using the previously published procedure[43]. Then the relationship between the lab frame and the molecular frame is derived from Euler rotation[27]. The tilt angle θ is then extracted using the neural network method outlined above, and the tilt angle was found to be ~23° (Figure 6).

Lastly, the ability of multimodal imaging in this platform[37] is shown (Figure 7). Here three different samples, namely, SDS@2β-CD, collagen, and L-phenylalanyl-L-phenylalanine (FF), are studied with the microscope with brightfield, SHG, and VSFG imaging modalities. First of all, all samples showed similar morphologies across different imaging modalities. Both SHG and VSFG showed intensity variations spatially, which is missing from optical images. Because SHG and VSFG both require ordered non-centrosymmetric structures, the variation in signal intensity could come from variations in local molecular ordering or molecular orientations. Unlike SHG, one can tune the MIR beam of VSFG to be resonant with different vibrational modes. In the case shown here, CH_x vibrational modes were studied at 3.5 μm and Amid-I mode at 6 μm. For FF, VSFG images with strong and uniform signals were obtained, suggesting a well-ordered self-assembled structure for all vibrational groups – agreeing with its crystalline nature. In contrast, the collagen sample displayed a stronger VSFG signal in the CH_x region over the Amide region, indicating the samples are flexible and their vibrational groups have different degrees of order.

DISCUSSION:

The most critical steps are from 1.42 to 1.44. It is critical to align the objective lens well for an optical spatial resolution. It is also important to collect the emitted signal, relay, and project the scanning beam as a line at the entrance slits. Proper alignments would guarantee the best resolution and signal-to-noise ratio. For a typical sample, like SDS@2β-CD 100 μm by 100 μm sheets, a good resolution image (~1 μm resolution) with a high signal-to-noise ratio would take 20 min. This is already faster than the previous version of the instrument[24,26]. Further enhancement of data acquisition speed can be realized by a higher repetition rate laser.

The current limitation is spatial resolution, which could be further improved with even higher NA objective optics and potential nonlinear optics-based super-resolution techniques[45]. Heterodyne detection has been applied in VSFG spectroscopy to resolve its phase and extract the molecular orientations[5,46–48]. This is technically doable in our experiment. However, VSFG imaging naturally relies on signal scattering off the sample, which scrabbles its phase and thereby complicates the relationships between molecular orientation and the phase of the VSFG signal.

Imaging the morphology of materials with chemical specificity is challenging because many imaging techniques lack molecular sensitivities. Rapid hyperspectral VSFG microscopy fills this void by probing molecular vibrational signatures and revealing molecular alignments of mesoscale organized matter that are important in materials science, chemistry, and biology. In the future, the reflective nature of the illumination optics will enable other techniques to be integrated into the core instrument, further increasing its capabilities and enabling multimodal images of chemical, biological, and material samples.

Supplementary Material

Refer to Web version on PubMed Central for supplementary material.

ACKNOWLEDGMENTS:

The instrument development is supported by Grant NSF CHE-1828666. ZW, JCW and WX are supported by the National Institutes of Health, National Institute of General Medical Sciences, Grant 1R35GM138092-01. BY is supported by the Youth Innovation Promotion Association, Chinese Academy of Sciences (CAS, 2021183).

REFERENCES:

(1). Zhu XD; Suhr H; Shen YR Surface vibrational spectroscopy by infrared-visible sum frequency generation. Physical Review B. 35 (6), 3047–3050 (1987).

(2). Shen YR Surface properties probed by second-harmonic and sum-frequency generation. Nature. 337 (6207), 519–525 (1987).

(3). Li Y; Shrestha M; Luo M; Sit I; Song M; Grassian VH; Xiong W Salting up of proteins at the air/water interface. Langmuir., 35 (43), 13815–13820 (2019). [PubMed: 31584824]

(4). Wang C; Li Y; Xiong W Extracting molecular responses from ultrafast charge dynamics at material interfaces. Journal of Materials Chemistry C. 8 (35), 12062–12067 (2020).

(5). Nihonyanagi S; Mondal JA; Yamaguchi S; Tahara T Structure and dynamics of interfacial water studied by heterodyne-detected vibrational sum-frequency generation. Annual Review of Physical Chemistry. 64 (1), 579–603 (2013).

(6). Nihonyanagi S; Yamaguchi S; Tahara T Ultrafast dynamics at water interfaces studied by vibrational sum frequency generation spectroscopy. Chemical Reviews. 117 (16), 10665–10693 (2017). [PubMed: 28378588]

(7). Singh PC; Nihonyanagi S; Yamaguchi S; Tahara T Ultrafast vibrational dynamics of water at a charged interface revealed by two-dimensional heterodyne-detected vibrational sum frequency generation. The Journal of Chemical Physics. 137 (9), 094706 (2012). [PubMed: 22957585]

(8). Jubb AM; Hua W; Allen HC Environmental chemistry at vapor/water interfaces: insights from vibrational sum frequency generation spectroscopy. Annual Review of Physical Chemistry. 63 (1) 107–130 (2012).

(9). Ishiyama T; Sato Y; Morita A Interfacial structures and vibrational spectra at liquid/liquid boundaries: molecular dynamics study of water/carbon tetrachloride and water/1,2-dichloroethane interfaces. The Journal of Physical Chemistry C. 116 (40), 21439–21446 (2012).

(10). Sapi A; Liu F; Cai X; Thompson CM; Wang H; An K; Krier JM; Somorjai GA Comparing the catalytic oxidation of ethanol at the solid-gas and solid-liquid interfaces over size-controlled pt nanoparticles: striking differences in kinetics and mechanism. Nano Letters. 14 (11), 6727–6730 (2014). [PubMed: 25337984]

(11). Chen X; Wang J; Sniadecki JJ; Even MA; Chen Z Probing α-helical and β-sheet structures of peptides at solid/liquid interfaces with SFG. Langmuir. 21 (7), 2662–2664 (2015).

(12). Dramstad TA; Wu Z; Gretz GM; Massari AM Thin films and bulk phases conucleate at the interfaces of pentacene thin films. The Journal of Physical Chemistry C. 125 (30), 16803–16809 (2021).

(13). Xiang B; Li Y; Pham CH; Paesani F; Xiong W Ultrafast direct electron transfer at organic semiconductor and metal interfaces. Science Advances. 3 (11), e1701508 (2017). [PubMed: 29159282]

(14). Livingstone RA; Nagata Y; Bonn M; Backus EHG Two types of water at the water-surfactant interface revealed by time-resolved vibrational spectroscopy. Journal of the American Chemical Society. 137 (47), 14912–14919 (2015). [PubMed: 26544087]

(15). Wagner JC; Hunter KM; Paesani F; Xiong W Water capture mechanisms at zeolitic imidazolate framework interfaces. Journal of the American Chemical Society. 143 (50), 21189–21194 (2021). [PubMed: 34878776]

(16). Montenegro A; Dutta C; Mammetkuliev M; Shi H; Hou B; Bhattacharyya D; Zhao B; Cronin SB; Benderskii AV Asymmetric response of interfacial water to applied electric fields. Nature. 594 (7861), 62–65 (2021). [PubMed: 34079138]

(17). Nihonyanagi S; Ishiyama T; Lee T; Yamaguchi S; Bonn M; Morita A; Tahara T Unified molecular view of the air/water interface based on experimental and theoretical $\chi(2)$ spectra of an isotopically diluted water surface. Journal of the American Chemical Society. 133 (42), 16875–16880 (2011). [PubMed: 21899354]

(18). Shen YR; Ostroverkhov V Sum-frequency vibrational spectroscopy on water interfaces: polar orientation of water molecules at interfaces. Chemical Reviews. 106 (4), 1140–1154 (2006). [PubMed: 16608175]

(19). Hosseinpour S; Roeters SJ; Bonn M; Peukert W; Woutersen S; Weidner T Structure and dynamics of interfacial peptides and proteins from vibrational sum-frequency generation spectroscopy. Chemical Reviews. 120 (7), 3420–3465 (2020). [PubMed: 31939659]

(20). Wang H; Xiong W Vibrational sum-frequency generation hyperspectral microscopy for molecular self-assembled systems. Annual Review of Physical Chemistry.72 (1), 279–306 (2021).

(21). Wang H-F; Velarde L; Gan W; Fu L Quantitative sum-frequency generation vibrational spectroscopy of molecular surfaces and interfaces: lineshape, polarization, and orientation. Annual Review of Physical Chemistry. 66 (1), 189–216 (2015).

(22). Inoue K; Ahmed M; Nihonyanagi S; Tahara T Reorientation-induced relaxation of free oh at the air/water interface revealed by ultrafast heterodyne-detected nonlinear spectroscopy. Nature Communications. 11 (1), 5344 (2020).

(23). Wang H; Gao T; Xiong W Self-phase-stabilized heterodyne vibrational sum frequency generation microscopy. ACS Photonics. 4 (7), 1839–1845 (2017).

(24). Wang H; Xiong W Revealing the molecular physics of lattice self-assembly by vibrational hyperspectral imaging. Langmuir. 38 (10), 3017–3031 (2022). [PubMed: 35238562]

(25). Raghunathan V; Han Y; Korth O; Ge N-H; Potma EO Rapid vibrational imaging with sum frequency generation microscopy. Optics Letters. 36 (19), 3891 (2011). [PubMed: 21964132]

(26). Wang H; Wagner JC; Chen W; Wang C; Xiong W Spatially dependent h-bond dynamics at interfaces of water/biomimetic self-assembled lattice materials. Proceedings of the National Academy of Sciences. 117 (38), 23385–23392 (2020).

(27). Wagner JC; Wu Z; Wang H; Xiong W Imaging orientation of a single molecular hierarchical self-assembled sheet: the combined power of a vibrational sum frequency generation microscopy and neural network. The Journal of Physical Chemistry B. 126 (37), 7192–7201 (2022). [PubMed: 36098975]

(28). Han Y; Hsu J; Ge N-H; Potma EO Polarization-sensitive sum-frequency generation microscopy of collagen fibers. The Journal of Physical Chemistry B. 119 (8), 3356–3365 (2015). [PubMed: 25614936]

(29). Chung C-Y; Potma EO Biomolecular imaging with coherent nonlinear vibrational microscopy. Annual Review of Physical Chemistry. 64 (1), 77–99 (2013).

(30). Potma EO Advances in vibrationally resonant sum-frequency generation microscopy. In Optics in the Life Sciences Congress; OSA: Washington, DC, 2017; p NM4C.2. 10.1364/NTM.2017.NM4C.2.

(31). Han Y; Raghunathan V; Feng RR; Maekawa H; Chung C-YY; Feng Y; Potma EO; Ge N-HH Mapping molecular orientation with phase sensitive vibrationally resonant sum-frequency

generation microscopy. The Journal of Physical Chemistry B. 117 (20), 6149–6156 (2013). [PubMed: 23675654]

(32). Hsu J; Haninnen A; Ge N-H; Potma EO Molecular imaging with sum-frequency generation microscopy. In Optics in the Life Sciences; OSA: Washington, DC, 2015; p NT4C.4. 10.1364/NTM.2015.NT4C.4.

(33). Hanninen A; Shu MW; Potma EO Hyperspectral imaging with laser-scanning sum-frequency generation microscopy. Biomedical Optics Express. 8 (9), 4230 (2017). [PubMed: 28966861]

(34). Wang H; Chen W; Wagner JC; Xiong W Local ordering of lattice self-assembled SDS@2β-CD materials and adsorbed water revealed by vibrational sum frequency generation microscope. The Journal of Physical Chemistry B. 123 (29), 6212–6221 (2019). [PubMed: 31247140]

(35). Cimatu K; Baldelli S Chemical imaging of corrosion: sum frequency generation imaging microscopy of cyanide on gold at the solid–liquid interface. Journal of the American Chemical Society. 130 (25), 8030–8037 (2008). [PubMed: 18517198]

(36). Shah SA; Baldelli S Chemical imaging of surfaces with sum frequency generation vibrational spectroscopy. Accounts of Chemical Research. 53 (6), 1139–1150 (2020). [PubMed: 32437170]

(37). Wagner Jackson C. Wu Zishan, Xiong W Multimodal nonlinear vibrational hyperspectral imaging. ChemRxiv. 10.26434/chemrxiv-2023-6d253 (2023).

(38). Yan C; Wagner J; Wang C; Ren J; Lee C; Wan Y; Wang S; Xiong W Multi-dimensional widefield infrared-encoded spontaneous emission microscopy: distinguishing chromophores by ultrashort infrared pulses. ChemRxiv. DOI: 10.26434/chemrxiv-2023-jfjvp (2023).

(39). Lin Y; Fromel M; Guo Y; Guest R; Choi J; Li Y; Kaya H; Pester CW; Kim SH Elucidating interfacial chain conformation of superhydrophilic polymer brushes by vibrational sum frequency generation spectroscopy. Langmuir. 38 (48), 14704–14711 (2022). [PubMed: 36394829]

(40). Choi J; Lee J; Makarem M; Huang S; Kim SH Numerical simulation of vibrational sum frequency generation intensity for non-centrosymmetric domains interspersed in an amorphous matrix: a case study for cellulose in plant cell wall. The Journal of Physical Chemistry B. 126 (35), 6629–6641 (2022). [PubMed: 36037433]

(41). Matlab Image Processing Toolbox Hyperspectral Imaging Library. Release 2022b, The Mathworks, Inc., Natick, MA USA Google Scholar.

(42). Armstrong BH Spectrum line profiles: the Voigt function. Journal of Quantitative Spectroscopy and Radiative Transfer. 7 (1), 61–88 (1967).

(43). Wu Z; Xiong W Neumann's principle based eigenvector approach for deriving non-vanishing tensor elements for nonlinear optics. The Journal of Chemical Physics. 157 (13), 134702 (2022). [PubMed: 36209027]

(44). Chollet F Keras Neural Network Library. https://github.com/fchollet/keras (accessed Apr 12, 2021).

(45). Vicidomini G; Bianchini P; Diaspro A STED super-resolved microscopy. Nature Methods. 15 (3), 173–182 (2018). [PubMed: 29377014]

(46). Xiong W; Laaser JE; Mehlenbacher RD; Zanni MT Adding a dimension to the infrared spectra of interfaces using heterodyne detected 2D sum-frequency generation (HD 2D SFG) spectroscopy. Proceedings of the National Academy of Sciences. 108 (52), 20902–20907 (2011).

(47). Lukas M; Backus EHG; Bonn M; Grechko M Passively stabilized phase-resolved collinear sfg spectroscopy using a displaced sagnac interferometer. The Journal of Physical Chemistry A. 126 (6) 951–956, 2022. [PubMed: 35113564]

(48). Ji N; Ostroverkhov V; Chen C; Shen Y Phase-sensitive sum-frequency vibrational spectroscopy and its application to studies of interfacial alkyl chains. Journal of the American Chemical Society. 129 (33), 10056–10057 (2007). [PubMed: 17661466]

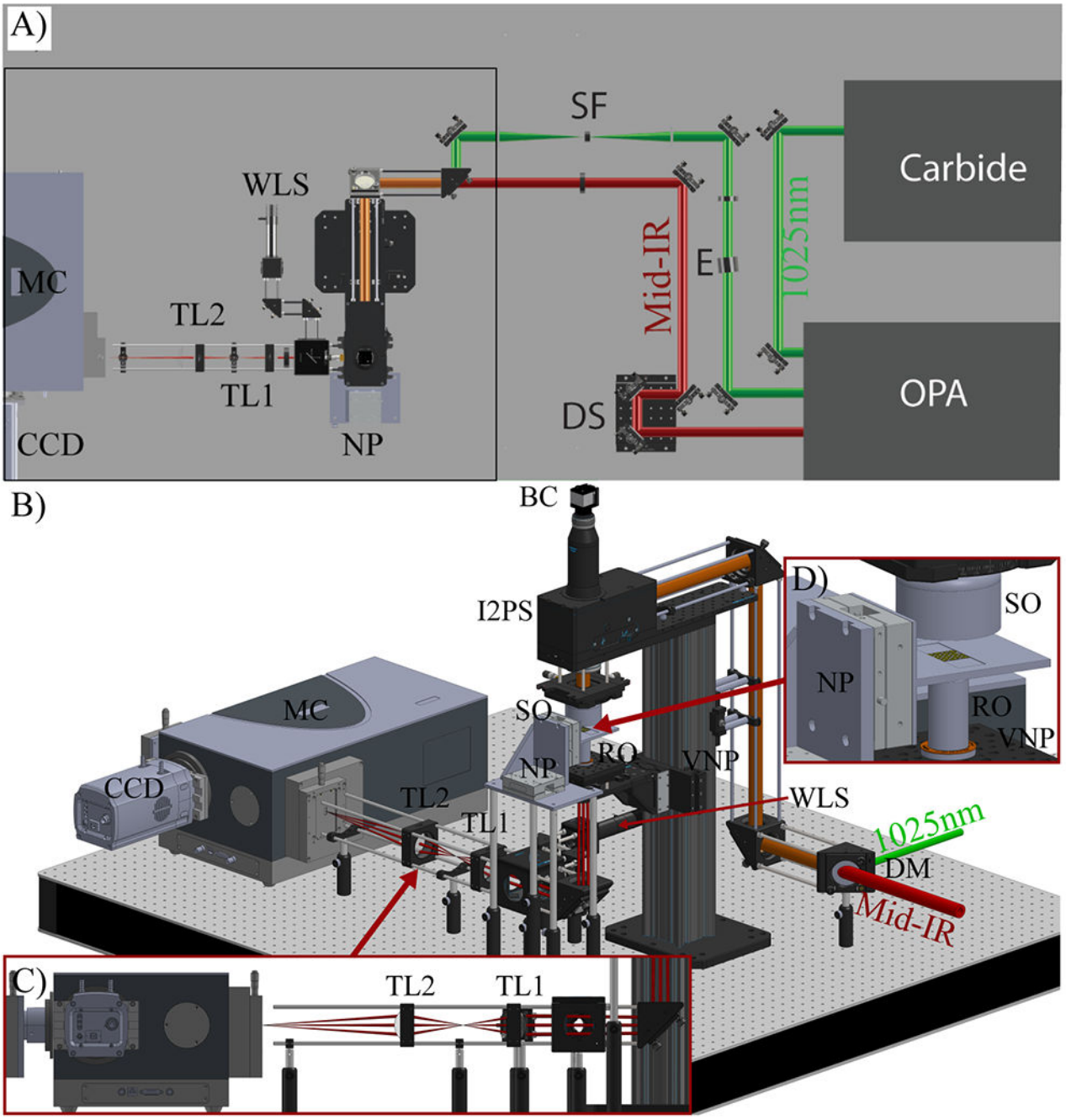

Figure 1: Multimodal hyperspectral VSFG microscope.

(**A**) **Top view of the core setup.** A 1025 nm pump laser was sent to an OPA to generate a tunable mid-IR pulse. The residual 1025 nm was frequently narrowed by an etalon (E) and spatially filtered into a Gaussian beam by a spatial filter (SFG). Mid-IR and 1025 nm beams are spatially overlapped at a customized dichroic mirror (DM) and guided through the inverted microscope (boxed region in **A**). (**B**) The two beams are sent to a 325 Hz resonant beam scanner mounted to an integrated 2-position slider (I2PS), enabling seamless switching between brightfield and nonlinear optical modalities. The microscope platform is

equipped with a reflective-based infinity-corrected Schwarzschild objective (SO) acting as a condenser and a refractive-based infinity-corrected imaging objective (RO) mounted to a vertical nanopositioning (VNP) z-axis stage. The SO focuses the line of incoming beams that the resonant beam scanner reflects onto the sample while the RO collects the VSFG line section of signals. It is important to fine-control the z-axis position of the RO at 1 μm precision to ensure the sample is at the best focal condition for high-quality imaging. The collimated line of the VSFG signal is then directed to a tube lens system composed of 2 tub lenses (TL1 and TL2), forming a magnified image at the entrance slit of the monochromator (MC). The frequency-resolved line of spectra is then hyperspectrally imaged on a charge-coupled device (CCD). After collecting each hyperspectral line, the sample is scanned in the axis perpendicular to the resonant beam scanner scanning axis using the NP. To collect bright field images of the sample, the I2PS is moved to the brightfield position, and a mirror intercepting the white light source (WLS) is installed. Light is then focused by the RO and imaged by the SO. An image is then formed at the sensor plane of the brightfield camera (BC) at the top of the inverted microscope. (**C**) Detailed view of the optical path through the tube-lens area into the MC and CCD. (**D**) Detailed view of the sample area between the SO and RO.

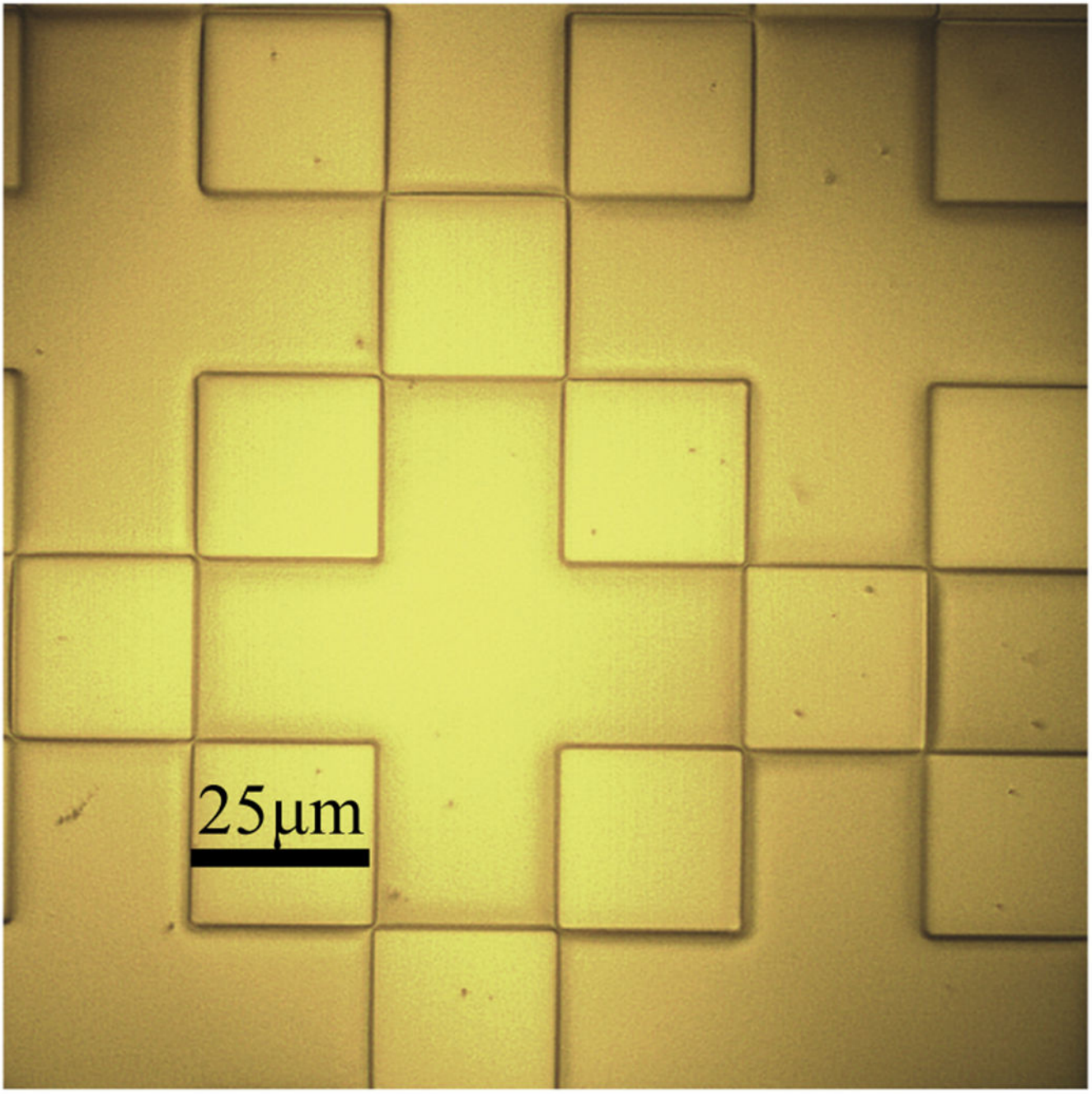

Figure 2:
Representative image quality for rough alignment of brightfield imaging modality of a ZnO pattern.

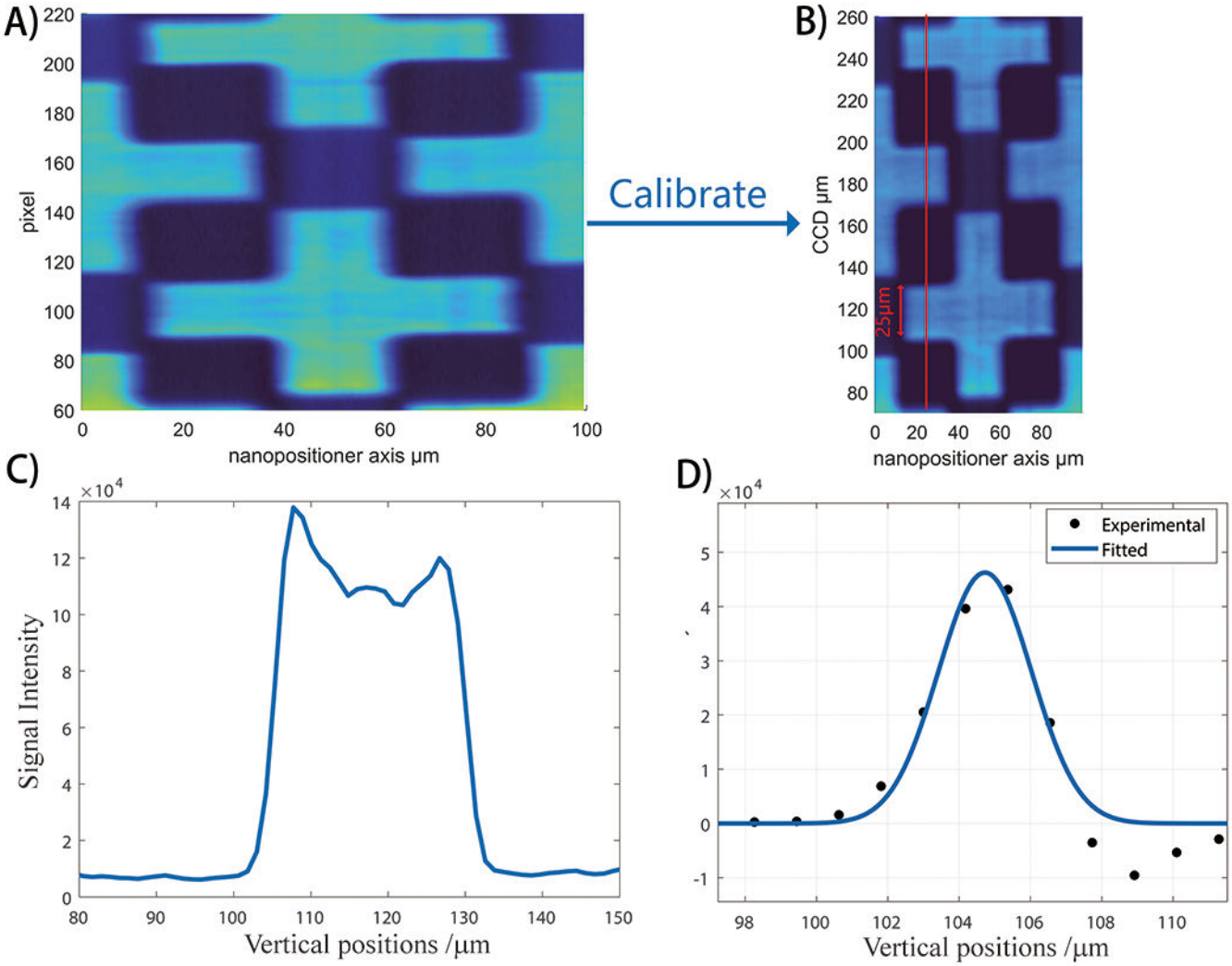

Figure 3: Vertical axis calibration workflow.

This figure illustrates how to convert the CCD pixels to vertical spatial dimensions in the unit of µm. (**A**) An image is collected and reconstructed of the ZnO patterned coverslip. Then, the pixel distance from one to the other edges of the pattern (small vertical bar in **A**). Because the ZnO pattern cross is designed to have a 25 µm width, one can use the ratio of physical width to pixel width here to calculate the physical/pixel dimension ratio. A representative, vertical axis calibrated image is shown in (**B**). **(C)** Lastly, a vertical slice is taken as indicated by the red line. (**D**) The derivative of the vertical slice is taken to obtain the spatial resolution. The derivative of the vertical slice is used to obtain the spatial resolution.

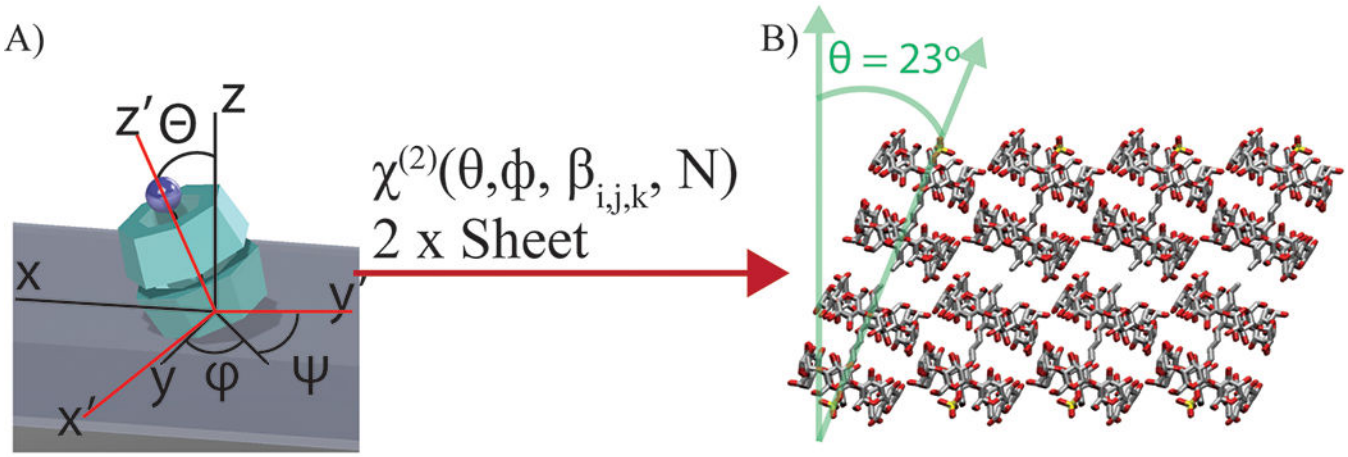

Figure 4: Illustration of Euler transformation.

(**A**) Illustration of the Euler transformation between the laboratory coordinates (XYZ) second-order susceptibility $\chi^{(2)}$ and the molecular coordinates (xyz) hyperpolarizability β_{ijk}. z-y′-z″ Euler rotation is performed on the molecular coordinates, with ϕ as the in-plane rotation angle, θ as the tilt angle, and ψ as the twist angle. ψ is integrated out for arbitrary twist angles about the molecular axis. ϕ is not integrated out because all molecules rotate to a specific angle relative to the lab frame to form the self-assembled sheets. N is the relative surface coverage of the two sheets. (**B**) Visualization of the tilted subunits forming a sheet determined by the neural network results. This figure has been modified from Wagner et al.[27].

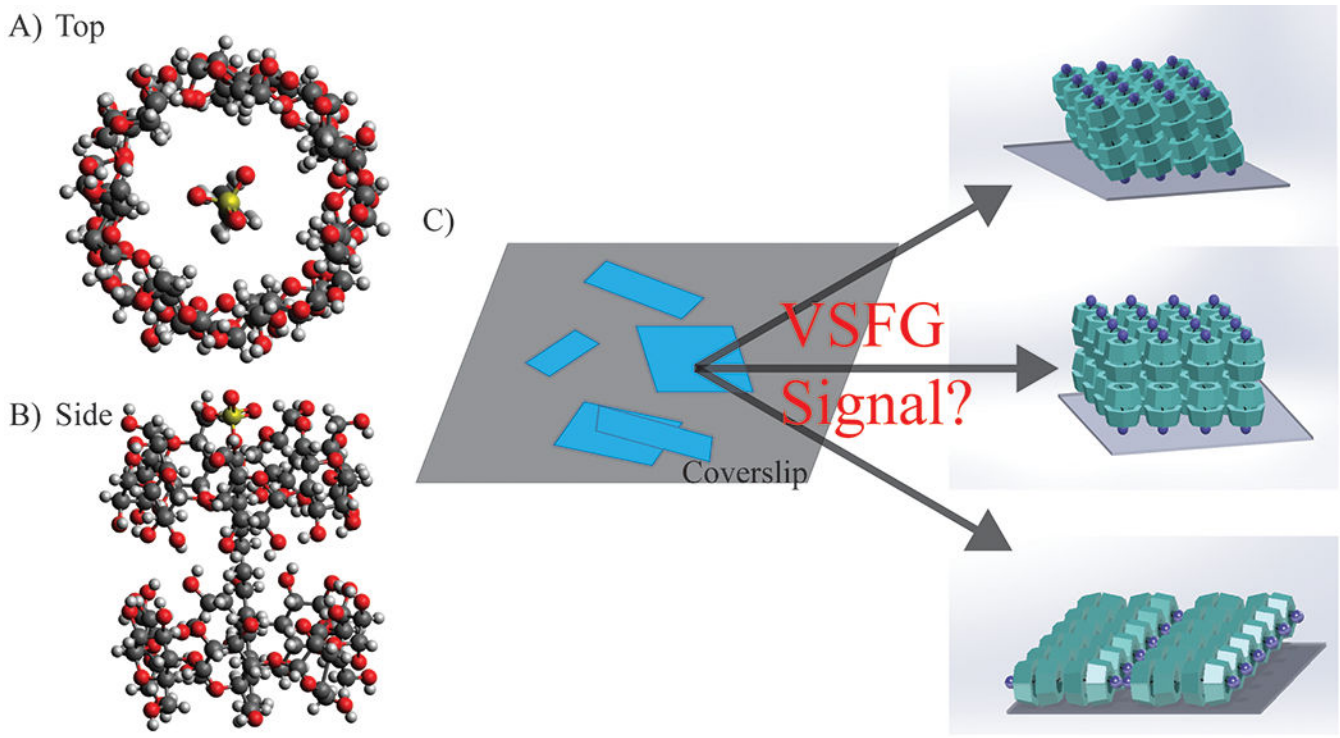

Figure 5: Molecular structure, morphology and potential orientation of SDS@β-CD.
(**A**) Top-view and (**B**) side-view chemical structure of SDS@β-CD. (**C**) Representative heterogeneous sample distribution of the mesoscale sheets on the sample plane. The molecular subunit could have different orientations and alignment on the substrate, which is unknown. This figure has been modified from Wagner et al.[27].

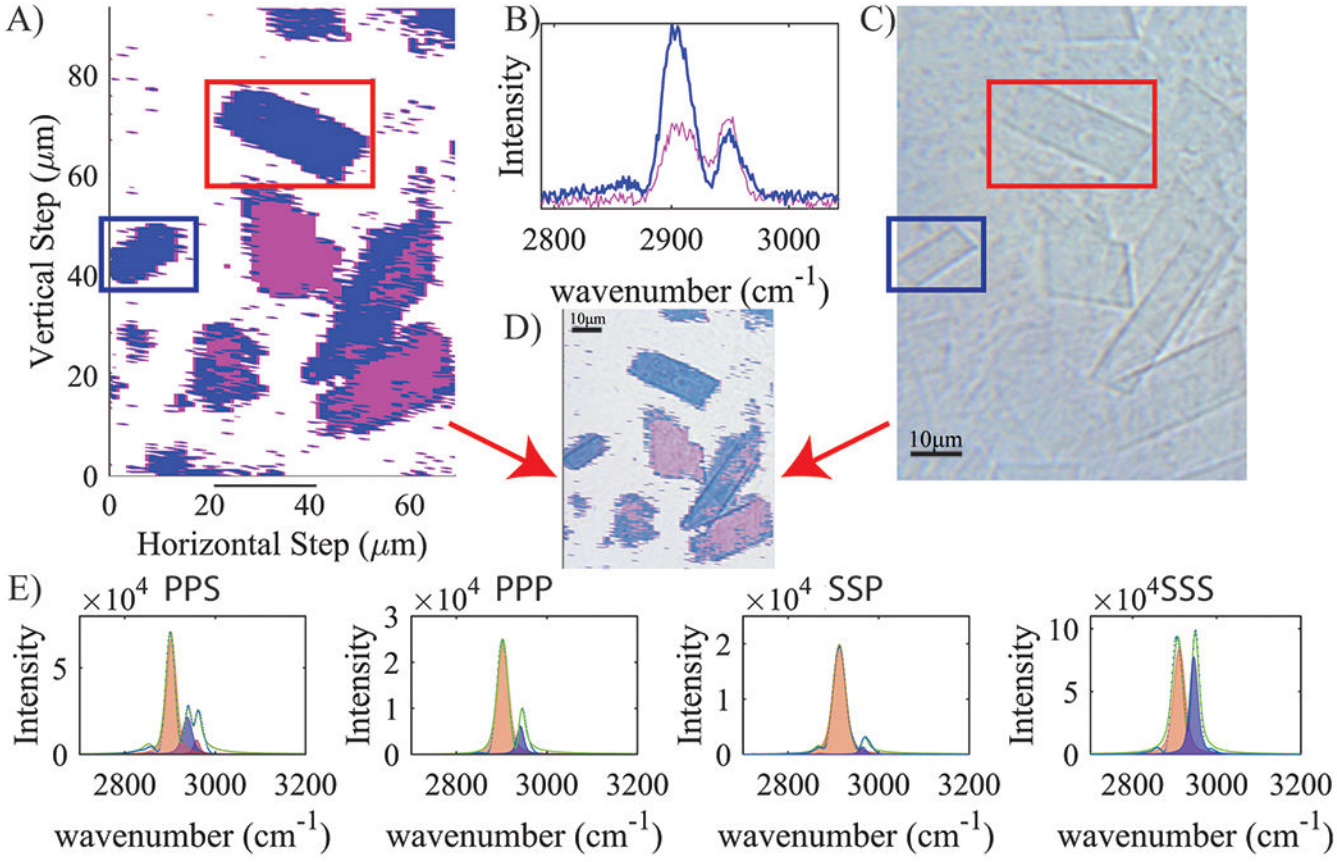

Figure 6: Polarization resolved VSFG image overlay with brightfield modality.

(**A**) Polarization resolved (SSS) hyperspectral VSFG image of SDS@2β-CD. Purple and pink colors represent areas where different spectra reside, and the corresponding spectra are plotted in (**B**), which are representative spectra for single pixels with signal-to-noise ratio for blue and magenta spectra ~56 and ~26, respectively. The sheets in the red and blue boxes are analyzed explicitly below to extract the supramolecule tilt angles. (**C**) Brightfield image of the same area as that in (**A**). (**D**) VSFG hyperspectral image overlayed with an optical image of an identical area. (**E**) From left to right: PPS, PPP, SSP, and SSS polarization resolved spectra summed over 180 and 480 pixels within the two single sheets highlighted in red and blue boxes in (**A**). All spectra had a dominant feature centered at approximately 2910 cm^{-1} and a signal-to-noise ratio in the order of 1000. The spectra were fitted with multiple Voigt functions, which were represented by the shaded areas, and used for further orientation analysis. This figure has been modified from Wagner et al.[27].

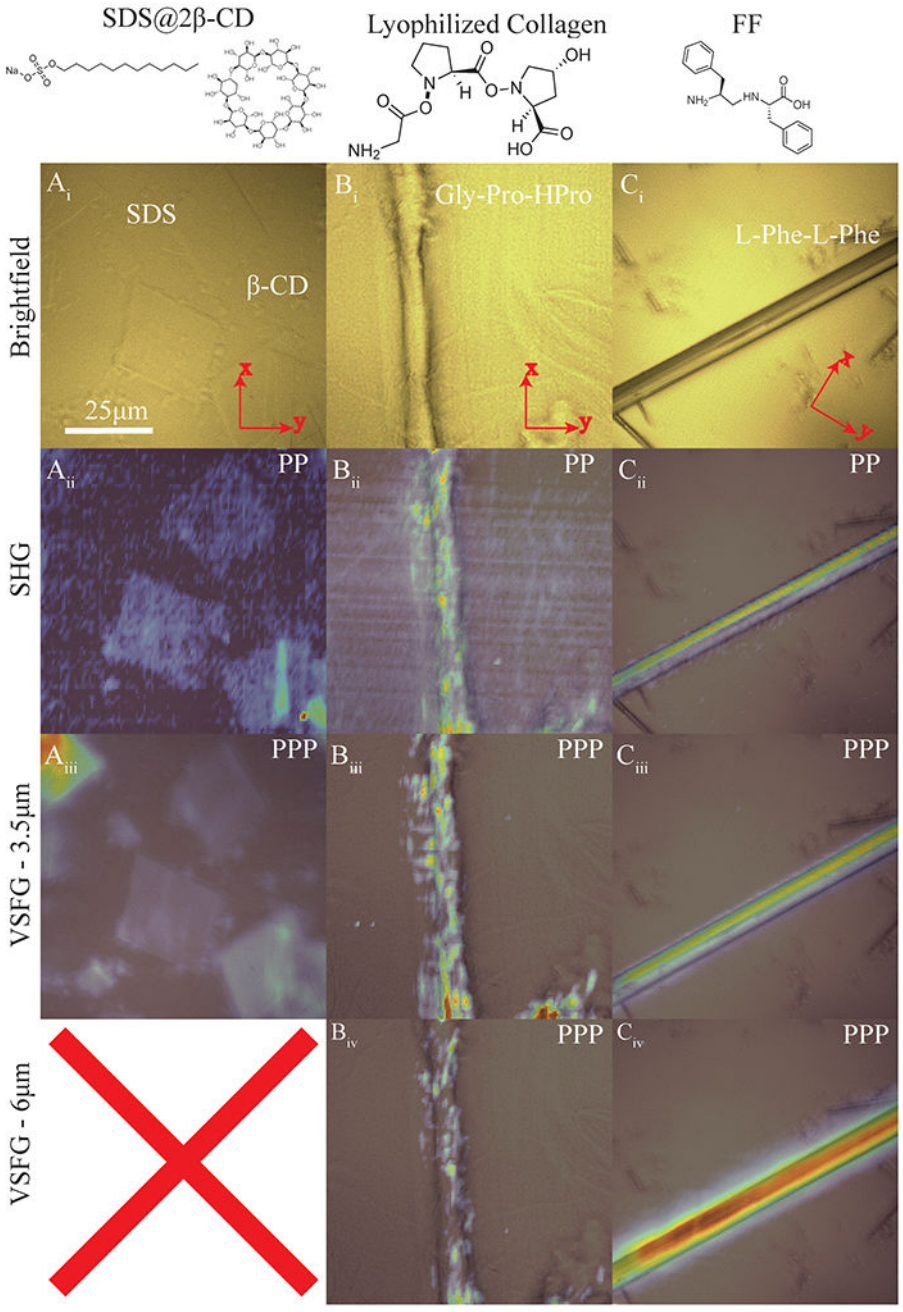

Figure 7: Multimodal images of three different samples.

(A_i–A_{iii}) SDS@2β-CD brightfield, SHG (PP polarization) and, VSFG (PPP polarization) of 3.5 μm region images, respectively. Nonlinear images are overlaid with brightfield images. Chemical structures of SDS and 2β-CD are shown in the inset of **a_i**. (**B_i–B_{iv}**) Lyophilized collagen brightfield, SHG (PP polarization), VSFG (PPP polarization) of 3.5 μm and 6 μm regions respectively. The chemical structure of the primary protein trimer residue of collagen, composed of glycine, proline, and hydroxyproline, is shown in the inset of **B_i**. (**C_i-C_{iv}**) FF brightfield, SHG (PP polarization), and VSFG (PPP polarization) of 3.5 μm and

6 μm regions respectively. The chemical structure for the FF molecular subunits is shown in the inset of **c_i**. All 6 μm images are taken under a purged nitrogen instrument environment to remove attenuation from ambient air moisture. SDS@2β-CD does not have a VSFG image at 6 μm because it does not have Amid groups.

J Vis Exp. Author manuscript; available in PMC 2024 March 01.

Table of Materials

Name of Material/ Equipment	Company	Catalog Number	Comments/Description
CCD	Andor Technologies	Newton	2D CCD for frequency and spatial resolution
Yb doped Solid State Laser	Light Conversion	CB3-40W	Seed laser
Collinear Optical Parametric Amplifier	Light Conversion	Orpheus-One-HP	Tunable MID light generator
RGB Color CCD Camera	Thorlabs	DCU224C	Brightfield camera, discontinued but other cameras will work just as well
Infinity Corrected Refractive Objective	Zeiss	420150-9900-000	Refractive Objective
Infinity Corrected Schwarzschild Objective	Pike Technologies Inc.	891-0007	Reflective objective
Monochromator	Andor Technologies	Shamrock 500i	Provides frequency resolution for each line scan
Nanopositioner	Mad City Labs Inc.	MMP3	3D sample stage
Resonant Scanner	EOPC	SC-25	325Hz resonant beam scanner
Whitelight Source	Thorlabs	WFA1010	Whitelight illumination source for brightfield imaging
Cage Plate Mounting Bracket	Thorlabs	KCB2	hold and adjust mirrors at a precise angle
25.0mm Right-Angle Prism Mirror, Protected Gold	Thorlabs	MRA25-M01	reflect light and produce retroreflection, redirecting light back along its original path
Right Angle Kinematic Mirror Mount, 30mm	Thorlabs	KCB1	hold and adjust mirrors at a precise angle
Right Angle Kinematic Mirror Mount, 60mm	Thorlabs	KCB2	hold and adjust mirrors at a precise angle
X-Y Axis Translation Stage w/ 360 deg. Rotation	Thorlabs	XYR1	precise movement and positioning of objects in two dimensions, along with the ability to rotate the platform
Ext to M32 Int Adapter	Thorlabs	SM1A34	provide compatibility and facilitating the connection between components with different thread types
60mm Cage Mounting Bracket	Thorlabs	LCP01B	mount and position a 60 mm cage system in optical setups
1X Camera Por	Thorlabs	WFA4100	connect a camera to a microscope or optical system
XY(1/2″) Linear Translator with Central SM1 Thru Hole	Thorlabs	XYT1	provide precise movement and positioning in two dimensions
Visible LED Set	Thorlabs	WFA1010	provide illumination in imaging setup
60mm Cage Mounted Ø50.0mm Iris	Thorlabs	LCP50S	control the amount of light passing through an optical system
SM2, 60mm Cage Arm for Cerna Focusing Stage	Thorlabs	CSA2100	securely mount and position condensers
500mm Tall Cerna Body with Epi Arm	Thorlabs	CEA1500	provide the function of enabling top illumination techniques in microscopy
M32x0.75 External to M27x0.75 Internal Engraving	Thorlabs	M32M27S	adapt or convert the threading size or type of microscope objectives
M32x0.75 External to Internal RMS	Thorlabs	M32RMSS	adapt or convert the threading size or type of microscope objectives
Right Angle Kinematic Breadboard	Thorlabs	OPX2400	incorporate a sliding mechanism with two fixed positions

Name of Material/ Equipment	Company	Catalog Number	Comments/Description
Manual Mid-Height Condenser Focus Module	Thorlabs	ZFM1030	adjust the focus of an optical element
3″ Universal Post Holder-5 Pack	Thorlabs	UPH3-P5	hold and support posts of various sizes and configurations
XT95 4in Rail Carrier	Thorlabs	XT95RC4	mount and position optical components
Snap on Cage Cover for 60mm Cage, 24in Long,	Thorlabs	C60L24	enclose and protect the components inside the cage
30 mm to 60 mm Cage Plate, 4 mm Thick	Thorlabs	LCP4S	convert between a 30 mm cage system and a 60 mm cage system
Air spaced Etalon	SLS Optics Ltd.	Customized	generate narrow-band 1030nm light
WPH05M-1030 - Ø1/2″ Zero-Order Half-Wave Plate, Ø1″ Mount, 1030 nm	Thorlabs	WPH05M-1030	alter the polarization state of light passing through it
WPLQ05M-3500 - Ø1/2″ Mounted Low-Order Quarter-Wave Plate, 3.5 μm	Thorlabs	WPLQ05M-3500	alter the polarization state of light passing through it
X axis Long Travel Steel Extended Contact Slide Stages	Optosigma	TSD-65122CUU	positioning stages that offer extended travel in the horizontal (X) direction
Customized Dichroic Mirror	Newport	Customized	selectively reflects or transmits light based on its wavelength or polarization
Motorized module with 1″ Travel for Edge-Mounted Arms	Thorlabs	ZFM2020	control the vertical positon of the imaging objective
Three-Chnnale Controller and Knob Box for 1″ Cerna Travel Stages	Thorlabs	MCM3001	control ZFM2020
Laser	Carbide, Light-Conversion	C18212	Laser source
Tube lens	Thorlabs	LA1380-AB - N-BK7	SFG signal collection
RGB tube lens	Thorlabs	**ITL200**	white light collection